

Radar Cross Section of Orbital Debris Objects

Yu-Lin Xu⁽¹⁾, Timothy Kennedy⁽²⁾, and Eugene Stansbery⁽³⁾

⁽¹⁾ University of Texas at El Paso - Jacobs JETS Contract, NASA Johnson Space Center, Mail Code XI5-9E, Houston, TX 77058, USA, yu-lin.xu-1@nasa.gov

⁽²⁾ NASA Johnson Space Center, Mail Code XI5-9E, 2101 NASA Parkway, Houston, TX 77058, USA

⁽³⁾ Emeritus, NASA Johnson Space Center, Mail Code XI5-9E, 2101 NASA Parkway, Houston, TX 77058, USA

ABSTRACT

This discussion is concerned with the radar-data analysis and usage involved in the building of model orbital debris (OD) populations in the near-Earth environment, focusing on radar cross section (RCS). While varying with radar wavelength, physical dimension, material composition, overall shape and structure, the RCS of an irregular object is also strongly dependent on its spatial orientation. The historical records of observed RCSs for cataloged OD objects in the Space Surveillance Network are usually distributed over an RCS range, forming respective characteristic patterns. The National Aeronautics and Space Administration (NASA) Size Estimation Model provides an empirical probability-density function of RCS as a function of “effective diameter” (or “characteristic length”), which makes it feasible to predict possible RCS distributions for a given model OD population and to link data with model from a statistical perspective. The discussion also includes application of the widely used method of moments (MoM) and the Generalized Multi-particle Mie-solution (GMM) in the prediction of the RCS of arbitrarily shaped objects. Theoretical calculation results for an aluminum cube are compared with corresponding experimental measurements.

1 INTRODUCTION

Key observational data used in the building and updating of model orbital debris (OD) populations in the near-Earth environment for objects in millimeter and centimeter size ranges includes radar measurements of radar cross section (RCS), polarization, range, and range-rate. OD objects, such as satellite explosion and collision fragments, as well as small pieces generated from regular, non-violent processes of surface material degradation or from surface bombing of micrometeoroids and small debris particles, are mostly of irregular shape. In general, radar data does not provide directly and explicitly physical and geometrical measurements for a target, which are essential in the description and characterization of the debris populations. Instead, the desired information is complexly embedded in measured RCSs and polarizations. RCS is a property of a radar target’s reflectivity and does not necessarily bear a straightforward relationship with its geometrical cross-sectional area. For non-spherical objects, an object’s RCS may vary significantly with its spatial orientation presented to the radar beam. In reality, an observed RCS may well be attributed to objects of considerably different sizes, materials, shapes, or structures.

To relate RCS with object “size” in a practically beneficial way, NASA developed a Size Estimation Model (SEM), based on laboratory (mono-static) RCS measurements for a set of representative debris objects (hypervelocity impact fragments) over a range of radar frequencies and spatial orientations [1, 2]. The smooth curve in the SEM presents the orientation- and shape-averaged RCS as a monotonic function of target “SEM-size.” When having a large number of RCS measured for an OD object by a radar over a time period, such as in the case of cataloged objects tracked in the Space Surveillance Network (SSN), the one-to-one RCS-to-SEM-size mapping according to the SEM smooth curve will provide a fairly good estimate for the size of the object based on mean or median RCS. In addition, for a large set of RCS data, obtained with the radar operating in the beam-park (or staring) mode, the standard SEM converts the RCSs to a rough size distribution, as a first approximation. It is emphasized that, besides the simplified one-to-one averaged-RCS-to-SEM-size conversion, the NASA SEM provides an empirical probability-density function (PDF) of RCS for a given size. Such an informative PDF of RCS gives approximately the probability of measuring an RCS value conditioned on the size-to-wavelength ratio, which is useful for the modeling of OD populations based on staring-mode radar data. Given a radar and viewing geometry, the PDF of RCS helps to reasonably predict the RCS distributions for a model OD population, and to possibly improve the model by best matching model predictions with observed RCS distributions statistically.

Reliable theoretical prediction of the RCS demands an accurate exposition of the intricate interaction between radiation and matter. Theoretical approaches exist that are applicable to solving radiative scattering by arbitrary

material bodies. A widely used numerical approach is the method of moments (MoM) or boundary element method (BEM). As applied to electromagnetic scattering problems, it was originally proposed in [3]. The MoM requires only the discretization of surface rather than volume and is a powerful alternative to the popular finite element method. The Generalized Multi-particle Mie-solution (GMM) [4-6] is a rigorous radiative scattering theory for arbitrary multi-body systems, which has a special version, GMM-PA, applicable specifically to periodic structures [7-9]. The GMM-PA provides a feasible way to study the scattering by an arbitrarily shaped body through a characteristic, finite periodic array (PA) comprising a huge number of identical component units. This is to put together a large amount of mass “points” to represent a material body and takes into account the intricate interaction of scattered radiation among the constituent elements. Using a cubic electric conductor as an example, theoretical predictions generally agree with published experimental data. Some basic considerations and implications in applying the MoM and GMM in RCS predictions are briefly discussed.

2 RADAR CROSS SECTIONS OBSERVED IN TRACKING AND STARING MODES

The SSN tracks large ($\geq \sim 10$ cm) objects in the near-Earth environment. The recorded historical RCS measurements for cataloged objects generally show a probability-density distribution. Given a specific radar, the orientation- and shape-dependences are the main causes responsible for the observed pattern of RCS variation, aside from random observation errors. The RCS distribution pattern is closely connected with the shape and structure of an object. Figure 1 shows two examples for the probability-frequency distributions of the observed RCSs of catalog objects. The observed RCSs shown include data up to April 5, 2019.

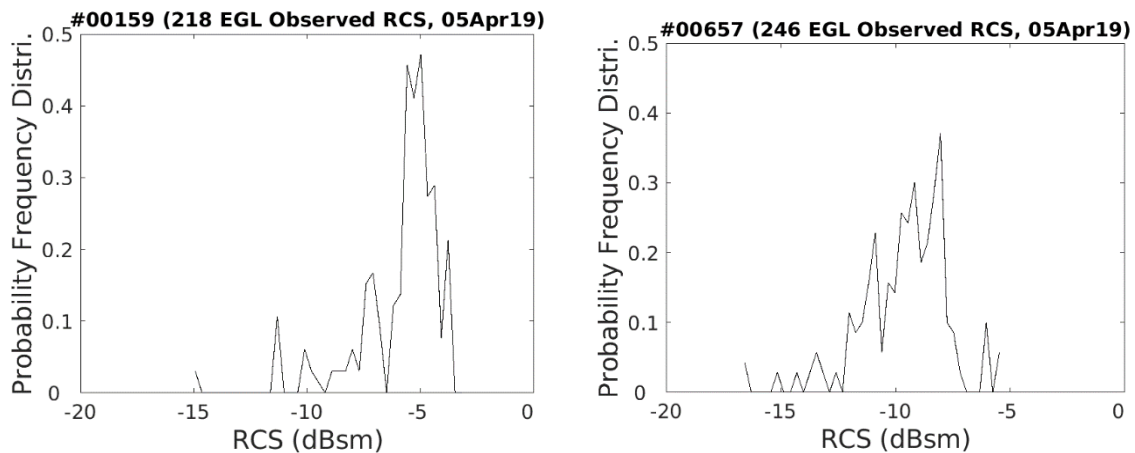


Fig. 1. Probability frequency distribution of the RCSs, the Eglin radar observed until April 05, 2019, for two breakup fragments, the SSN catalog objects with Sat. ID# 00159 and 00657.

Unlike the large objects, radar detections of millimeter- and sub-centimeter OD objects are collected when the radar is operated in the staring mode, which are only small samplings from the vast OD environment. In the staring mode, an object stays in a radar's field of view for only a very short time. The RCS of a radar detection is assumed to be measured when its spatial orientation (i.e., the aspect angle the target presents to the radar beam) has no significant change due to the short time interval that the object is within the radar beam, while the orientation is an occurrence of chance for a tumbling, irregular object. Figure 2 shows the distributions of total RCS and circular polarization over altitude for all detections with total RCS ≥ -60.73 dBsm (equivalent to “SEM-size” ≥ 3.16 mm) in the HUSIR data set of calendar year (CY) 2014, collected with the radar, HUSIR, pointing to 75° elevation and East [10]. Displayed in Fig. 2 are detection number-density distributions with bin-sizes of 20 km for altitude, 1 dBsm for RCS, and 2.5% for the polarization. As it is well known, due to mainly the unique polarization properties of homogeneous and isotropic spheres in exact back-scattering, the special family of sodium-potassium (NaK) droplets can be identified and extracted from radar detections [11,12]. Shown in Fig. 3 is the cumulative distribution of RCS for HUSIR 75° E data of CY 2014 and 2015 after the removal of NaK detections, referred to as “NoNaK.” An appropriate use of a radar data set concerns the limiting size inherent in the data. The HUSIR radar is limited in detection sensitivity to target sizes roughly $> \sim 5$ mm at altitudes under ~ 1000 km and has an issue of detection efficiency at high altitudes for sizes $< \sim 1$ cm.

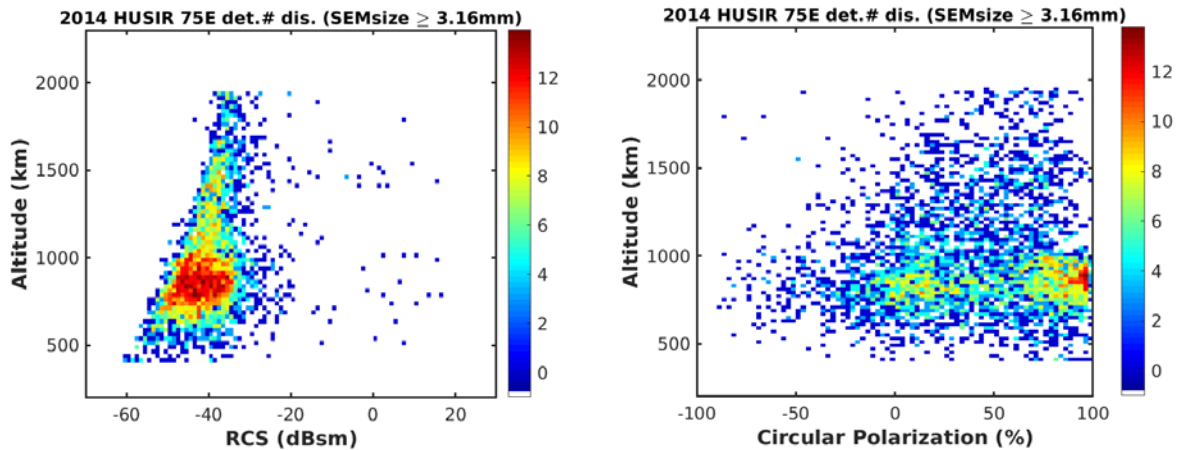


Fig. 2. HUSIR data of CY2014, 75°E: altitude versus total RCS (left) and circular polarization (right). Displayed are number-density distributions.

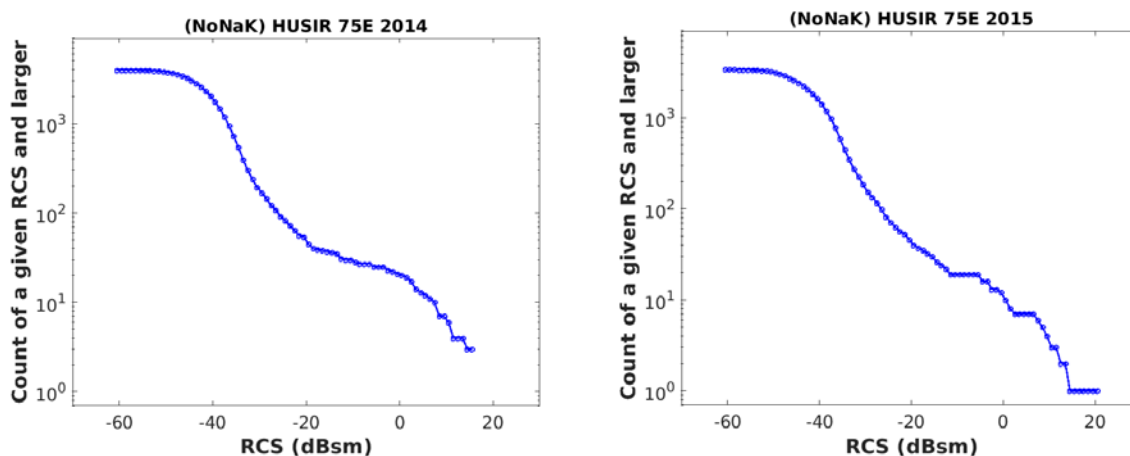


Fig. 3. Cumulative RCS distribution of HUSIR 75°E data of CY 2014 (left) and 2015 (right). The data shown are after the removal of NaK detections.

3 RADAR-DETECTION AND RCS PREDICTION FOR A MODEL OD POPULATION

In the modeling of OD populations, observed RCS distributions are compared against model predictions to inspect and improve models. A model population consists of a large number of earth orbits. The probability of an object being detected by a radar for a given viewing geometry in the staring mode is determined by the orbital parameters and the number of objects on the orbit. The prediction of the RCS of the possible detection requires taking into account the probability-density distribution of RCS for the specified “size” of the objects on an orbit. Currently available for use in such RCS predictions are the NASA SEM provided empirical probability distributions of RCS.

3.1 Empirical probability-density distribution of RCS provided in the NASA SEM

The NASA SEM provided empirical probability-density function of RCS, as a function of wavelength-normalized size, is a size-dependent linear combination of gamma and log-normal distribution densities, derived from the large set of static laboratory RCS measurements, the RCS database of the SEM [1]. The left panel of Fig. 4 shows these PDFs for the case when the transmitted radar wave is right-hand circularly polarized. Shown in the right panel of Fig. 4 are the PDFs for five individual values of wavelength-normalized size: 0.29, 0.51, 2.88, 9.12, and 28.8.

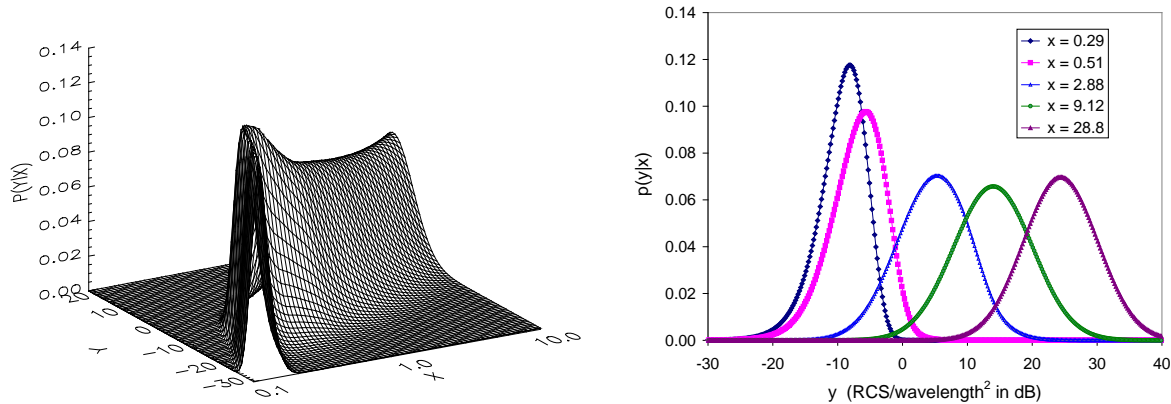


Fig. 4. Probability distribution functions (PDFs), $p(y|x)$, of circular-polarization RCS, provided in NASA SEM, where $x = \text{size}/\lambda$, y is RCS/λ^2 in dB, and λ is radar wavelength (left), and the PDFs at the discrete values of $x = 0.29, 0.51, 2.88, 9.12,$ and 28.8 (right).

3.2 Model OD populations

There are different ways to build model populations for different size regimes. Critical evolutionary source-models, such as LEGEND [13, 14], provide benchmark model OD populations in the modeling of the OD environment. LEGEND attempts to reproduce and mimic all known historical breakup (BU) events, creating explosion or collision fragments down to 1 mm in size, based on the NASA Standard Breakup Model (SBM) [15] for the majority of the BU events in the large-scale background. For some BU events, believed to be extraordinary, LEGEND allows to use specific custom scaling factors other than the common one that the 2001 NASA SBM recommends. In LEGEND, all objects are propagated forward to a desired time. Figure 5 shows the object-number density distributions of the LEGEND ≥ 1 cm model population of June 2014 in the two-dimensional orbital parameter spaces of eccentricity versus perigee altitude (left panel), and eccentricity versus inclination (right panel).

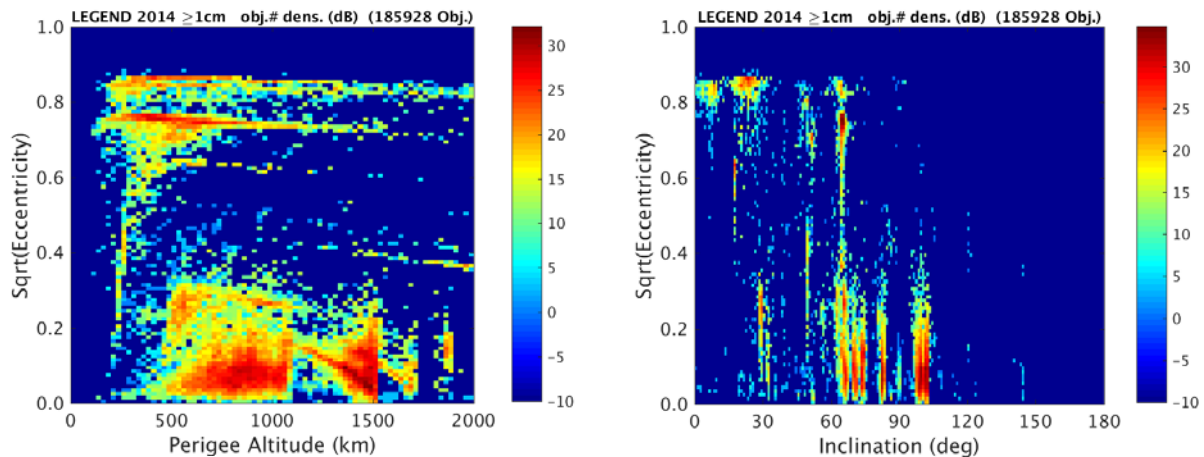


Fig. 5. Object-number density distribution of LEGEND ≥ 1 cm model population (June 2014) in the two-dimensional space of eccentricity versus perigee altitude (left) and eccentricity versus inclination (right).

3.3 An example for the comparison of radar-observed and model-predicted RCS distributions

Depending on the size distribution in specified earth orbits, a model OD population has its specific, expected staring-mode RCS distribution for a radar pointing to a given direction. Since an object of a given size may contribute to a range of possible observed RCS, the RCS prediction relies on a best available PDF of RCS to estimate the probability of being observed for a specific RCS. Given a limiting value of RCS and its corresponding SEM-size (i.e., the size converted from the smooth SEM curve for the given RCS), objects of size smaller than the SEM-size will have contributions to the RCSs greater than the limiting RCS. Figure 6 shows the cumulative RCS

distribution in HUSIR 75°E data of CY 2014, together with the model-predicted contribution from the LEGEND population of 2014. The predictions shown in the left panel for a given RCS include contributions only from objects of size > the corresponding SEM-size, while those shown in the right panel include also contributions from objects of size smaller than the SEM-size. Note that, besides LEGEND model populations, the HUSIR data include contributions from some other special types of component OD families that are treated outside LEGEND.

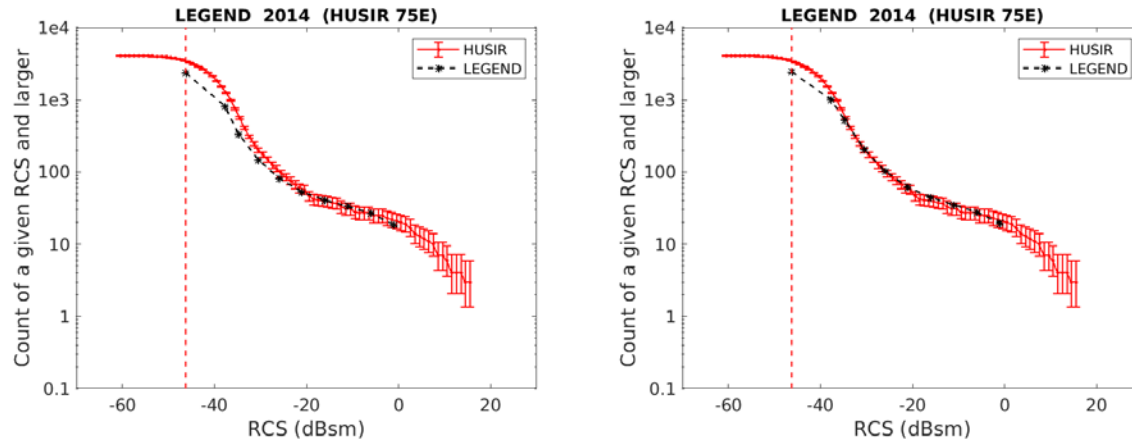


Fig. 6. Cumulative distribution of RCS in HUSIR CY2014 75E data (shown together with Poisson limits at the single-side confidence level of 84.13%) compared with the model-predicted contribution from the partially scaled LEGEND population of 2014. The predictions shown in the left panel for a given RCS include contributions only from objects of size > the corresponding SEM-size, while those shown in the right panel also include contributions from objects of sizes smaller than the SEM-size.

4 THEORETICAL AND EXPERIMENTAL STUDY OF RCS

Both experimental and theoretical studies of RCS are beneficial to deepening our insight in RCS data analysis. The comparison between experimental results and theoretical predictions is an effective way to test and validate theory or theoretical models. However, strictly speaking, the test is mutual. The theoretical investigation of RCS, studying the scattering characteristics of objects and calculating desired scattering quantities at arbitrary points of interest, enables visualization of the scattered spatial distributions and surface current on electrically conducting bodies. It is profitable to conduct parametric studies using a theoretical versus strictly measurement-based approach in the optimization of theoretical models. Many different methods are available for the theoretical analysis purposes. These include the finite element method (FEM), finite-difference time domain (FDTD), the Finite Integration Technique (FIT), the MoM – and their many variants, the Multiple-Sphere T-matrix (MSTM) [16], the GMM, the Discrete Dipole Approximation (DDA) [17], and others. As always, every theoretical or numerical solution method has its regime of validity and limitations in practical applications. This section briefly discusses the application of the MoM and GMM in RCS predictions, using an aluminum cube as the illustrative example for the comparison between theoretical and experimental results.

4.1 The Method of Moments (MoM)

As applied in the radiative scattering area, the MoM is a full wave solution technique to Maxwell's equations, with many different academic, government, and commercial implementations available. The MoM software used to study radar scattering phenomenon in this paper is the Electromagnetic Interactions GENEralized (EIGER) software [18]. EIGER was developed in collaboration with Lawrence Livermore National Laboratory, Sandia National Laboratory, University of Houston, US Navy Space and Naval Warfare Systems Command, and NASA. It implements many of the popular MoM formulations including the Electric Field Integral Equation; Magnetic Field Integral Equation; Combined Field Integral Equation; Poggio, Miller, Chew, Harrington, Wu, and Tsai (PMCHWT) formulation for dielectric materials, as well as hybrid BEM and FEM formulations. EIGER has been successfully applied to both radar scattering and antenna radiation problems with a few representative examples depicted in Figure 7 [19-21]. It has been characterized extensively and compared with measurements over many different projects conducted by the software development organizations, and the underlying methods are widely used in commercial software tools [22,23].

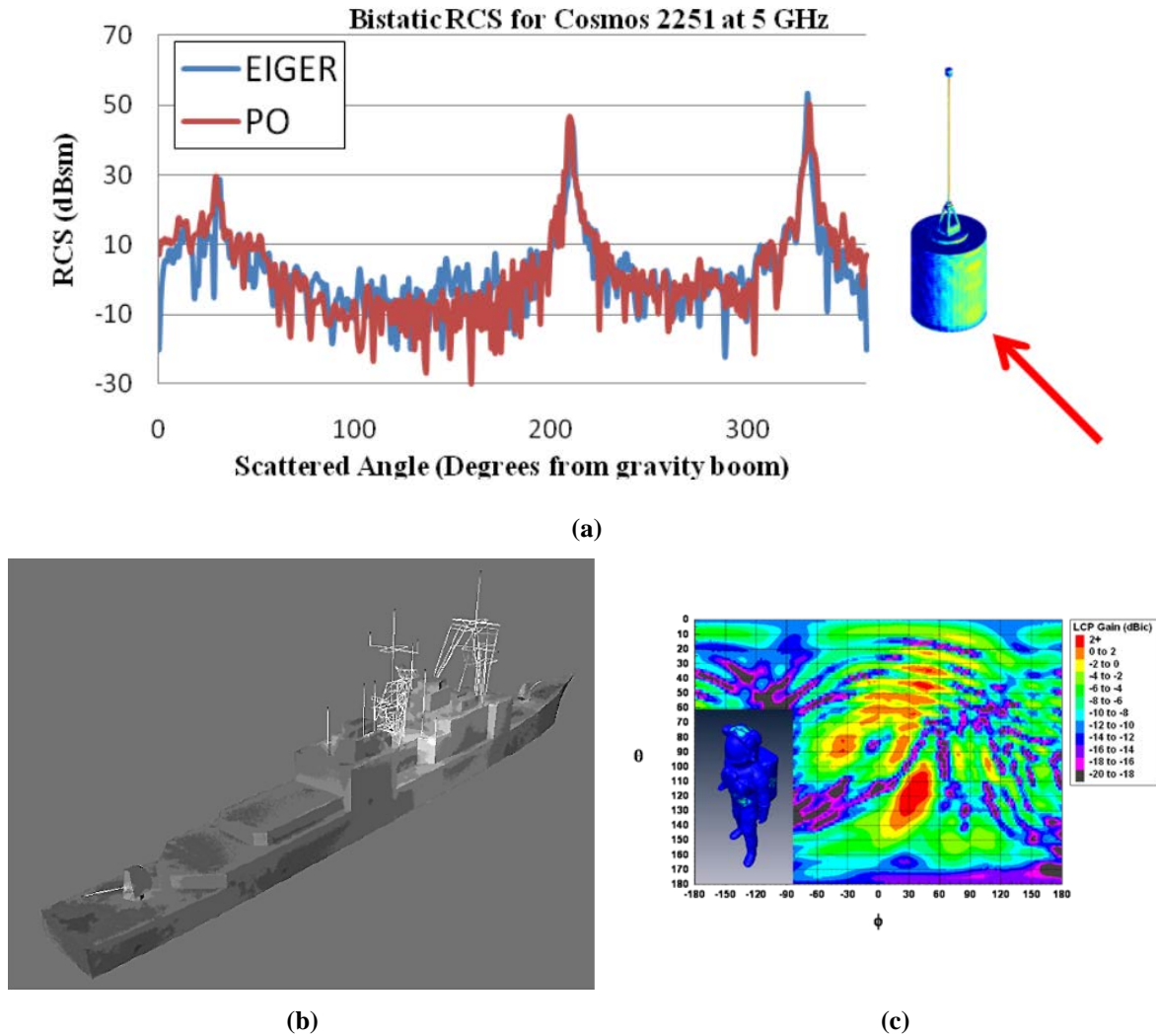


Fig. 7. Exemplars for radar scattering and radiation problems modeled by EIGER. The bistatic RCS for Cosmos 2251 at 5 GHz (a), surface currents induced by a dual whip antenna at 10 MHz (b), and the radiation pattern for an S-band, multi-antenna element beamformer on an EVA suit (c). Credit: (a) [19], Fig. 5, permission granted by the author Horsley, M., (b) [20], Fig. 4, permission granted by Naval Engineers Journal.

4.2 The Generalized Multi-particle Mie-solution (GMM) and its special version of GMM-PA

Analogous to the Lorenz-Mie theory for single homogeneous and isotropic spheres, there are well-established, comprehensive analytical solutions to the ensemble scattering of electromagnetic radiation. The GMM is such an extension from the classical Lorenz-Mie theory, a rigorous and complete solution to the electromagnetic scattering of a monochromatic plane wave by an arbitrary multi-body configuration, tested by some systematic experimental scrutiny [e.g., 24]. The computer codes of GMM (in FORTRAN) were released to the public in 2001. Literally, the general GMM approach does not place any restriction on the size, shape, material composition, structure, and morphology of the constituent units in an ensemble. It solves individual (or partial) scattered fields of all component scattering bodies in their respective, displaced coordinate systems, with scattered waves from all other components translated and added to the incident field for a given component unit. While the generality is advantageous on one hand, there are disadvantages in practical calculations on the other hand, as regards computing time requirements in particular. For an array consisting of N component particles, the required computing time is roughly proportional to N^2 . In practical calculations, this solution process becomes demanding in both computer power and computing time, when the number of component scattering bodies are not small (say, $\gg 10^3$ for wavelength-sized components).

Responses of bulk material to external sources of electromagnetic radiation are the cooperative reaction of its constituent subdivisions. The radiative scattering properties of a solid body are essentially the unified manifestation of all individual volume elements. To study the radiative scattering from an arbitrary, rigid material body, a practicable way is to substitute it with a characteristic, finite PA of densely packed, tiny particles, given an overall shape and macroscopic structure. This is conceivable especially when an individual component volume is sufficiently small so that the excited radiative field inside a component unit becomes homogeneous and the scattered field strength from such an individual constituent subdivision is proportional to its volume. As mentioned earlier, the GMM has a special version of GMM-PA developed recently, which is applicable specifically to periodic structures. The development of the special PA-approach relies on the favorable periodicity of the spatial structures of PAs combined with distinct features of GMM, such as the direct use of precise phase terms for both incident and scattered radiation when solving far-field scattering. It brings remarkable savings in computing time, in comparison with the standard GMM procedure. The GMM-PA approach opens a practicable way to probe radiative scattering properties of material bodies, either regular or irregular in shape, through a characteristic, finite PA comprising a huge number of identical component units.

As stressed in [7, 8], the special PA-formulation of GMM holds precise merely for PAs of infinite extents that have no edge (and thus lack practical meaning). For PAs of finite lengths, the tradeoff is that the “edge effect” introduces certain numerical errors into numerical solutions, the significance of which depends on the total number of replica units in a PA. As practical GMM-PA calculation results indicate, the edge effect recedes as the number of component particles in a PA increases. In other words, the PA-approach provides sufficiently accurate numerical solutions to the finite PAs that have a sufficiently large number of component unit cells. In principle, the GMM-PA places no restriction on the shape or structure of the individual component unit and the total number of the constituent units. The prerequisite is that the T -matrix [25, 26] of an individual scattering unit in independent scattering (i.e., when it is isolated) are known analytically (such as for homogeneous and isotropic spheres) or can be computed with a satisfactory precision for given physical and geometrical parameters. In addition, the size of the constituent unit may not be arbitrarily small as the GMM-PA formulation is classical and boundary conditions need to be well defined.

In the GMM-PA scattering calculations, there are some implications in the preparation of required input parameters. These involve basic considerations concerning the intrinsic properties of the bulk material of a scattering body. An example is the complex refractive index for both bulk material and the individual component particle. The refractive index of bulk material generally changes with incident wavelength. In many cases, the desired refractive index is not readily available. For instance, an online calculator provides the complex refractive index of aluminum up to the incident wavelength of 247.97 μm , which is 473.49+i524.58. The complex index of refraction is, however, a required input quantity that affects the reliability of the numerical solutions. Another example is the calculation of the skin depth in connection with the electrical conductivity, which is also important for the scattering calculations, especially for electric conductors.

In the work reported here, the formulation used to relate the complex refractive index and the electrical conductivity of a non-magnetic material is as follows [27]:

$$\sigma = \text{Re}(i\omega\varepsilon^*) = \frac{4\pi m' m''}{\lambda_0 \mu_0 c}, \quad (1)$$

where $i = \sqrt{-1}$, σ is electrical conductivity, ω is circular frequency, $\varepsilon = \varepsilon' + i\varepsilon''$ is the complex dielectric constant, the asterisk represents complex conjugate, $m = m' + im''$ is the complex refractive index, $m^2 = \varepsilon / \varepsilon_0$, ε_0 is the permittivity of free-space, λ_0 is wavelength in free space, μ_0 is the magnetic permeability of free space, and c is the speed of light. When the electrical conductivity is known, the product of $m' m''$ can be calculated for a given wavelength. For most metals, m' nearly equals to m'' at long wavelengths.

For an incident monochromatic plane wave of wavelength λ_0 in free space, the attenuation constant $\alpha/2$ (with α being the absorption coefficient) in the medium of the complex refractive index $m = m' + im''$ is simply

$$\frac{\alpha}{2} = \frac{2\pi m''}{\lambda_0}. \tag{2}$$

Based on the relation between the attenuation constant α and the skin depth δ_e , we have

$$\delta_e = 2\delta_p = \frac{2}{\alpha} = \frac{\lambda_0}{2\pi m''}, \tag{3}$$

where δ_p is the penetration depth. The skin effect becomes more apparent for good conductors as frequency increases, while it does not need to be taken into account for poor conductors or dielectric materials as far as the scattering calculations are concerned.

4.3 Theoretical prediction and the comparison between theoretical and experimental results

To demonstrate the application of the MoM and GMM-PA in RCS predictions, an aluminium cube with side length of 7 cm is used here as an example. Theoretical predictions are compared with experimental results. A linearly y-polarized monochromatic plane wave is incident broadside along the positive z-direction, with the y-axis parallel to four cube sides. This example is to show the wavelength dependence of RCS. The frequency of the incident plane wave ranges from 600 MHz to 18 GHz, and accordingly, the side length of the cube ranging from ~ 0.14 to 4 wavelength.

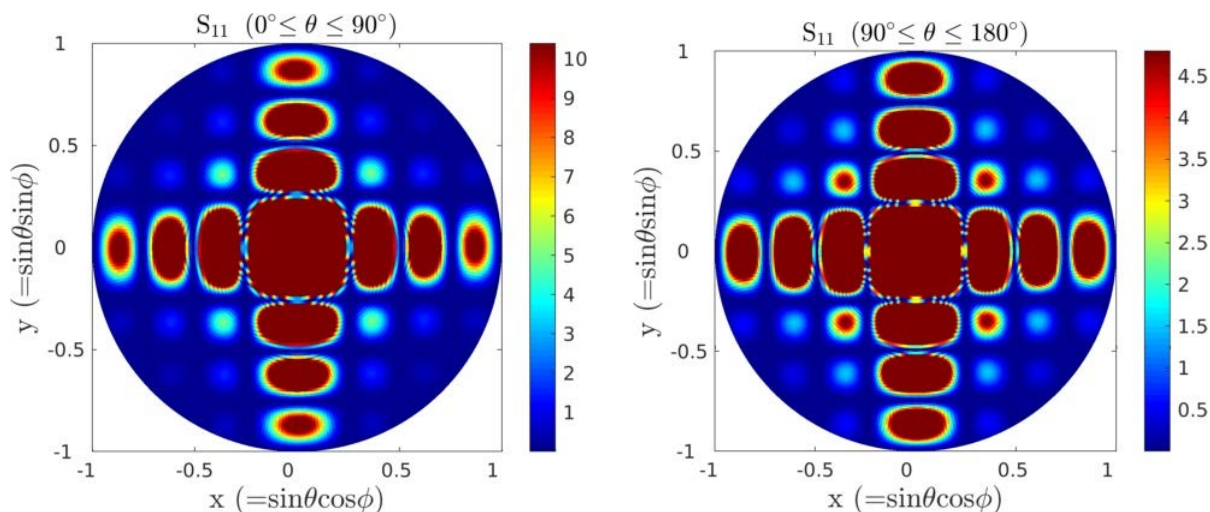


Fig. 8. Dependence of the Mueller matrix element S_{11} (i.e., the scattering intensity) on scattering angle θ and azimuth angle ϕ (shown as variation with $x = \sin\theta\cos\phi$ and $y = \sin\theta\sin\phi$) for the aluminum 7 cm cube under broadside incidence when the wavelength of the incident wave is 1.75 cm.

In the GMM-PA calculations, all six surfaces of the cube are replaced by a layer of identical, touching spheres, the radius of which equals to δ_e , the skin depth at a given incident wavelength. These spheres consist of the same bulk material of aluminum and have the same complex refractive index as the cube. The skin depth changes with incident wavelength, mostly proportional to the square root of the wavelength. When the frequency of the incident plane wave is 10 GHz, i.e., of wavelength 3 cm, the skin depth is $8.1473e-5$ cm and each surface is replaced by $\sim 7.4e+7$ tiny spheres. In the GMM-PA calculations, the cube is considered to consist of only these six sphere layers, i.e., hollow under the single-layer spheres. Figure 8 shows the GMM-PA computed angular distributions of the Mueller matrix element S_{11} (i.e., the scattered radiation normalized by incident intensity) of the aluminum cube in the forward and backward hemispheres at the incident wavelength of 1.75 cm. It is not surprising that the spatial distributions of the scattered far-field are similar to the far-field diffraction pattern of a square aperture. The RCS is connected with the exact backward direction, i.e., at the center of the backward-hemisphere plot (the right-side

panel). Note that, the spatial intensity distributions shown in Fig. 8 are with the peak projecting intensities in the central areas in both forward- and backward-scattering suppressed, in order to more clearly display the pattern of lower scattered-intensity distributions in the entire space other than the central area.

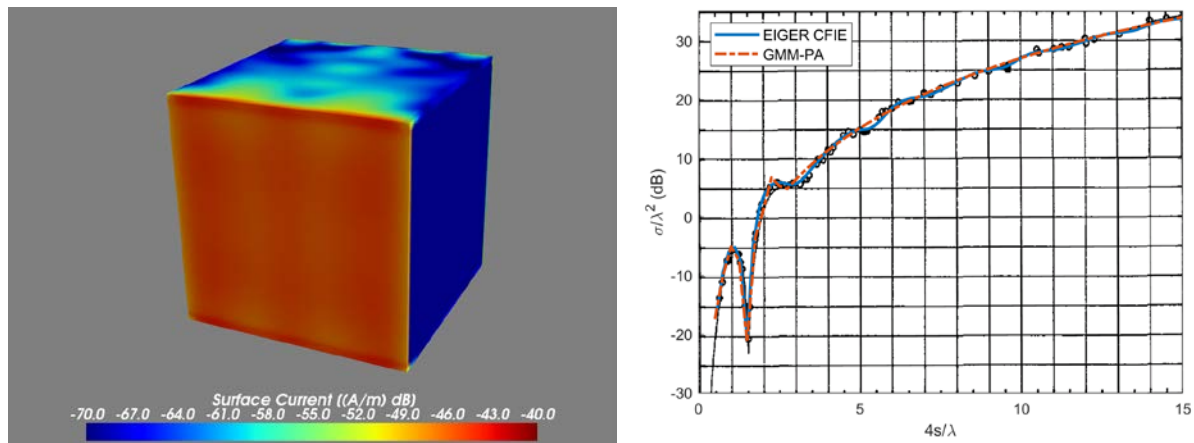


Fig. 9. (left) The MoM-predicted current distribution on the surface of the aluminum 7 cm cube at the incident wavelength of 3 cm, and (right) Broadside RCS of the aluminum 7 cm cube predicted from the MoM (EIGER simulations) and the GMM-PA approach. Black open circles are measured data [28].

The left panel of Fig. 9 shows the MoM-predicted surface current distribution for the y-polarized, broadside incident plane wave of wavelength 3 cm. In the right panel of Fig. 9, the MoM and GMM-PA predicted broadside RCSs for the aluminium cube of side length (s) 7 cm are compared with measured data [28]. The measured data was obtained at 11 X-band frequencies on 18 solid aluminium cubes varying in side length from 5 mm to 10 cm. Many theoretical models have been proposed to predict RCS of cubic electric conductors and to match the data, a summary for which can be found in [29]. Note that the GMM-PA predictions shown in the right panel of Fig. 9 include a couple of specific treatments when the parameter $4s/\lambda < 3$. When $4s/\lambda > 3$, the contribution to the predicted RCS mainly comes from the front surface, while the contribution from the back surface needs to add coherently when $4s/\lambda < 3$. In addition, when $4s/\lambda < 1.5$, the skin depth calculated from Eq. (3) needs to be enhanced by an adjustment factor proportional to the square root of λ . These need a convincing interpretation or clarification, which seems to involve both theoretical considerations and data collection. Recall that the data consists of RCS measurements for 18 cubes of different side lengths. In radiative scattering, the fundamental principle of electromagnetic similitude, implied in Maxwell equations, is valid only when refractive index remains the same. In reality, however, the complex refractive index of aluminium in the frequency range of the incident plane wave under study varies with the incident wavelength, proportional to the square root of the applied wavelength. The effect of the incident-wavelength dependence of the refractive index might be among those that require a further close inspection.

5 CONCLUSIONS

Important information on basic properties and structures of the large-scale OD environment is often inferred from observational data sampled under rather limited conditions. Radar data in the staring mode, indispensable to the modeling of small-size OD populations, basically are small groups of random samplings from the vast space. Most OD objects are irregular in shape, the RCS of which is strongly spatial-orientation dependent. The NASA SEM provides a probability-density distribution of RCS as a function of SEM-size, which is valuable for the prediction of RCS distributions probably observed from a model OD population. The comparison of such predicted RCS distribution with corresponding radar data helps to improve OD-population models.

Theoretical approaches exist for the theoretical study of the RCS of arbitrary solid material bodies. Two examples for them are briefly discussed. Experimental tests help to validate and possibly to improve theoretical models. The comparison between theoretical and experimental results also may help identify possible issues in the collection and usage of experimental data.

6 REFERENCE

1. Bohannon, G., Comparisons of Orbital Debris Size Estimation Methods Based on Radar Data, XonTech Report 920123-BE-2048, 1992.
2. Bohannon, G., Caampued, T., and Young, N., First Order RCS Statistics of Hypervelocity Impact Fragments, XonTech Report 940128-BE-2305, 1994.
3. Harrington, R.F., Field Computation by Moment Methods, Malabar, FL; Krieger Publishing, 1968.
4. Xu, Y.-L., Electromagnetic scattering by an aggregate of spheres, *Appl. Opt.*, Vol. 34, pp. 4573-4588, 1995.
5. Xu, Y.-L., Electromagnetic scattering by an aggregate of spheres: far field, *Appl. Opt.*, Vol. 36, pp. 9496-9508, 1997.
6. Xu, Y.-L., Electromagnetic by an aggregate of spheres: asymmetry parameter, *Phys. Lett. A*, Vol. 249, pp. 30-36, 1998.
7. Xu, Y.-L., Scattering of electromagnetic waves by periodic particle arrays, *J. Opt. Soc. Am. A*, Vol. 30, pp. 1053-1068, 2013.
8. Xu Y.-L., Scattering of electromagnetic radiation by three-dimensional periodic arrays of identical particles, *J. Opt. Soc. Am. A*, Vol. 31, pp. 322-331, 2014.
9. Xu, Y.-L., Fraunhofer diffraction of electromagnetic radiation by finite periodic structures with regular or irregular overall shapes, *J. Opt. Soc. Am. A*, Vol. 32, pp. 12-21, 2015.
10. Murray, J., Blackwell, C., Gaynor, J., Kennedy, T., "Haystack Ultra-wideband Satellite Imaging Radar Measurements of the Orbital Debris Environment: 2014 – 2017," NASA/TP-2019-220302, July 2019.
11. Stansbery, E.G., et al., Haystack Radar Measurements of the Orbital Debris Environment: 1990-1994, NASA JSC-27436, 1996.
12. Kessler, D.J., et al. A Search for a Previously Unknown Source of Orbital Debris: The Possibility of a Coolant Leak in Radar Ocean Reconnaissance Satellites, NASA JSC-27737, 1997.
13. Liou, J.-C., Hall, D.T., Krisko, P.H., and Opiela, J.N., LEGEND – a three-dimensional LEO-to-GEO debris evolutionary model, *Adv. Space Res.*, Vol. 34, pp. 981-986, 2004.
14. Liou, J.-C., Johnson, N.L., Risks in space from orbiting debris, *Science*, Vol. 311, pp. 340-341, 2006.
15. Johnson, N.L., Krisko, P.H., Liou, J.-C., Anz-Meador, P., NASA's New Breakup Model of EVOLVE 4.0, *Adv. Space Res.*, Vol. 28, pp. 1377-1384, 2001.
16. Mackowski, D.W., Analysis of radiative scattering for multiple sphere configurations, *Proc. R. Soc. London Ser. A*, Vol. 433, pp. 599-614, 1991.
17. Draine, B.T., and Flatau, P.J., Discrete-dipole approximation for periodic targets: theory and tests, *J. Opt. Soc. Am. A*, Vol. 25, pp. 2693-2703, 2008.
18. Sharpe, R.M., et al. EIGER: Electromagnetic Interactions GENEralized, IEEE Antennas and Propagation Society International Symposium, pp. 2366-2369, 1997.
19. Horsley, M., Fasenfest, B., A Parallel, High-Fidelity Radar Model, Proceedings of the 2010 AMOS Technical Conference, Maui, HI, 2010.
20. Rockway, J.W., et al. EM Design Technology for Topside Antenna System Integration, *Naval Engineers Journal*, Wiley, Vol. 113, pp. 33-43, 2001.
21. Kennedy, T.F., et al. Body-worn E-Textile Antennas: The Good, the Low-Mass, and the Conformal, *IEEE Transactions on Antennas and Propagation*, Vol. 57, pp. 910-918, 2009.
22. Jakobus, U., et al. "Method of moments accelerations and extensions in FEKO," 2011 International Conference on Electromagnetics in Advanced Applications, pp. 62-65.
23. Momentum 3D Planar EM Simulator, <https://www.keysight.com/en/pc-1887116/momentum-3d-planar-em-simulator?cc=US&lc=eng> (accessed August 2019).
24. Xu, Y.-L., and Gustafson, B.Å.S., A generalized multiparticle Mie-solution: Further experimental verification, *J. Quant. Spectrosc. Radiat. Transfer*, Vol. 70, pp. 395-419, 2001.
25. Waterman, P.C., Matrix formulation of electromagnetic scattering, *Proc. IEEE*, Vol. 53, pp. 805-812, 1965.
26. Waterman, P.C., New formulation of acoustic scattering, *J. Acoust. Soc. Am.*, Vol. 45, pp. 1417-1429, 1969.
27. Xu, Y.-L., et al. Calculation of the heat-source function in photophoresis of aggregated spheres, *Phys. Rev. E*, Vol. 60, pp. 2347-2365, 1999.
28. McGahan, R.V., Scattering experiments at the Ipswich Electromagnetic Measurements Facility: Backscatter from metal cubes, RADC TR-85-24, Feb. 1985.
29. Yaghjian, A.D., and McGahan, R.V., Broadside Radar Cross Section of the Perfectly Conducting Cube, *IEEE Transactions on Antennas and Propagation*, Vol. AP-33, pp. 321-329, 1985.